Synthesis of $BiOI/Bi_4O_5I_2/Bi_2O_2CO_3$ p-n-p heterojunctions with superior photocatalytic activities

Yin Peng*†, Pian-Pian Yu†, Hai –Yan Zhou† and An-Wu Xu*‡

Receipt/Acceptance Data **[DO NOT ALTER/DELETE THIS TEXT]**
Publication data **[DO NOT ALTER/DELETE THIS TEXT]**
DOI: 10.1039/b000000x [DO NOT ALTER/DELETE THIS TEXT]

Abstract: One-dimensional (1D) $BiOI/Bi_4O_5I_2/Bi_2O_2CO_3$ p-n-p heterojunction photocatalyst was synthesized by low-temperature solution method using Bi_2O_3 nanorods as sacrificial template. The formation mechanism of $BiOI/Bi_4O_5I_2/Bi_2O_2CO_3$heterostructure was discussed in detail according to the results of IR, XPS, TEM, SEM Mapping, XRD and SEM. Compared with pure BiOI, $Bi_2O_2CO_3$ and $Bi_4O_5I_2$, this ternary p-n-p heterojunction exhibited superior photodegradation efficiency of rhodamine B (100%) and methylene blue (97%) in 45 min under solar light irradiation, which was about 40, 25 and 10 times of pure BiOI, $Bi_2O_2CO_3$ and $Bi_4O_5I_2$, respectively. This enhanced photocatalytic performance was ascribed to the high separation rate of photo-generated carriers in the internal electric field due to the formation of p-n-p junctions and relatively large BET surface area (36.29 g/m^2). More importantly, 1D heterostructure is beneficial for transport of photo-generated electron-hole pairs and further improving the rate of photocatalytic reaction. Radical scavenger experiments revealed that the photo-generated holes were primarily active species in the photocatalytic system. This work would offer a new insight into the design and fabrication of ternary p-n-p junction structures for photocatalytic applications.

Introduction

Driven by increasing environmental pollutions and growing threat of current energy crisis, the search for cost-effective, sustainable and green energy sources to meet the global energy demands has attracted considerable research attention. Therefore, the exploration of highly active photocatalytic systems for directly harvesting and converting solar energy into usable energy format is one of the promising strategies, owing to its utilization of non-pollution and abundant sunlight as a source of energy. The semiconductor photocatalysts are widely used to split water into H_2 and O_2 [1,2], photoreduce CO_2 into renewable fuels, such as CH_3OH, CH_4, and CO[3-5], and decompose various organic contaminations to remedy our environment.[6,7] Many studies have been devoted to develop new and efficient photocatalysts.

The design of p-n heterostructure photocatalyst consisting of p-type and n-type semiconductors is one of the most common methods to improve efficiency of photocatalytic reaction.[8-11] With contact of p-type and n-type semiconductors each other, the bands of the semiconductors will bend and the Fermi levels will equilibrate because of the formation of a space charge region after the diffusion of electrons and holes.[8,9] Thus, the built-in electrical potential in the space charge region from n-type side to the p-type side can direct the electrons and holes to quickly travel at the opposite direction, and allow more effective separation and longer life-time of electron-hole pairs.[10,11] These advantages endow the p-n type heterostructures with an enhanced photocatalytic performance.

Bismuth oxyiodides belong to main group V–VI–VII ternary semiconductors with a special layered crystal structure. In the structure, positively charged $[Bi_2O_2]^{2+}$ slabs are interleaved by negative iodide slabs, resulting in an internal static electric field perpendicular to each layer. Such inherent electric fields are beneficial for facilitating the separation of photo-generated carriers. Therefore bismuth oxyiodides display promising photocatalytic performance due to their wide spectrum response and high efficiency. Bismuth oxyiodides have been studied widely, and their synthesis, modification, facet effects and photocatalytic mechanism have been reviewed by three articles.[12-14] Recently, some I-poor bismuth oxyiodides, such as $Bi_4O_5I_2$,[15-18] Bi_5O_7I,[18-22] $Bi_7O_9I_3$,[17,18,23,24] were synthesized and studied. It was proved that these I-poor bismuth oxyiodides displayed the better photocatalytic activity to degrade organic pollution than bismuth oxyiodides. In order to further improve the photocatlytic performance of I-poor bismuth oxyiodides, Li et al [25] synthesized $Bi_7O_9I_3$/reduced graphene oxide (RGO) composite by a facile solvothermal method. The $Bi_7O_9I_3$ nanoplates dispersed uniformly on RGO surface. The photocatalytic activity of $Bi_7O_9I_3$/RGO in degradation of RhB and phenol was 2.13 and 2.29 times that of pure $Bi_7O_9I_3$, respectively. The enhanced photocatalytic activity could be attributed to more effective charge transportations and separations, the high pollutant adsorption performance and the increased light absorption.

In this article, we report for the first time a ternary $BiOI/Bi_4O_5I_2/Bi_2O_2CO_3$ p-n-p heterojunction through low temperature aqueous phase method. $Bi_2O_2CO_3$ is an n-type semiconductor with a wide band gap (about 3.33 eV) and is beneficial for the formation of the p-n heterojunction with p-type BiOI and $Bi_4O_5I_2$. The experimental results also prove that this ternary p-n-p heterojunction system exhibits high photocatalytic activity to degrade RhB and MB dyes under solar light irradiation, superior to pure BiOI, $Bi_2O_2CO_3$ and $Bi_4O_5I_2$ samples. The enhanced photocatalytic activity is attributed to the effective separation of photo-generated electron-hole pairs due to the formation of p-n-p junction and relatively high surface area.

Experimental section

†The Key Laboratory of Functional Molecular Solids, Ministry of Education, College of Chemistry and Materials Science, Anhui Normal University, Wuhu 241000, China.
‡Division of Nanomaterials and Chemistry, Hefei National Laboratory for Physical Sciences at Microscale, Department of Chemistry, University of Science and Technology of China, Hefei 230026, P. R China.
Fax: (+86) 551-6360 2346; E-mail: anwuxu@ustc.edu.cn.

Photocatalyst preparation

All the reagents used in our experiment were analytical grade and used as received without further purification.

$Bi(OHC_2O_4)\cdot 2H_2O$ nanorods were synthesized according to our present report.[11] Bi $(NO_3)_3\cdot 5H_2O$ (2.911 g) and $Na_2C_2O_4$ (1.206 g) were dissolved separately in 20 mL distilled water. Then the $Na_2C_2O_4$ solution was added into the Bi $(NO_3)_3$ suspension solution with vigorous magnetic stirring. The mixed suspension solution was transferred into a stainless steel autoclave with a Teflon liner and heated at 120 ºC for 40 h. The obtained solid sample was washed with deionized water and anhydrous ethanol, and then dried at 60 ºC for 6 h. The Bi_2O_3 nanorods can be obtained by calcining $Bi(OHC_2O_4)\cdot 2H_2O$ nanorods at 400 ºC for 2 h.

$BiOI/Bi_4O_5I_2/Bi_2O_2CO_3$ samples were synthesized by low-temperature solution method. In a typical experiment, Bi_2O_3 nanorods (0.1 g) and KI (0.0094 g) were dispersed into deionized water (40 mL) under magnetic stirring for 30 min, and then $Bi(NO_3)_3\cdot 5H_2O$ (0.0276 g) was added. After further stirring for 30 min at room temperature, the mixture was transferred to the flask and heated at 80 ºC for 2 h. The obtained products were washed with anhydrous ethanol and deionized water, and dried at 60 ºC for 4 h. The sample was labelled S2 (the molar ratio of Bi_2O_3 : I^- : Bi^{3+} to 7.5 : 2 : 2). Change the molar ratio of Bi_2O_3 : I^- : Bi^{3+} to 7.5 : 3 : 3 and 7.5 : 1 : 1, the obtained products were labelled S3 and S1, respectively. For comparison, pure BiOI photocatalyst was also prepared by adopting the method mentioned above in the absence of Bi_2O_3.

$Bi_2O_2CO_3$ samples were synthesized according to ref 26. In a typical synthesis, $Bi(NO_3)_3\cdot 5H_2O$ (0.487 g) was added into 4 mL of concentrated nitric acid to form a clear solution after 10 min stirring at room temperature. Afterwards, 30 mL of deionized water, 0.8 g of polyvinylpyrrolidone (PVP) were added into the solution, and the mixture was vigorously stirred for 30 min to ensure that all reagents were dispersed homogeneously. Finally, hexamethylenetetramine (HMT) (0.9 g) was added into the solution and stirred for another 30 min. The resulting solution was transferred to a Teflon liner and heated at 180 ºC for 16 h. After being cooled down to room temperature, the precipitate was collected by centrifugation, washed with deionized water and anhydrous ethanol several times, and dried at 60 ºC for 6 h.

The $Bi_4O_5I_2$ nanoflakes were synthesized according to ref 16. In a typical synthesis, Bi $(NO_3)_3\cdot 5H_2O$ (0.728 g) and KI (0.498 g) were dissolved in 35 mL EG. Subsequently, 2 M NaOH was slowly dropped into the solution with stirring until the pH value of the solution reached 9.0. The solution was transferred into a Teflon-lined autoclave and heated at 150 ºC for 12 h. The obtained solid sample was washed with deionized water and anhydrous ethanol, and then dried at 60 ºC for 6 h.

Photocatalytic characterization

Field emission scanning electron microscopy (FE-SEM) images were recorded on a Hitachi S-4800 microscope. Transmission electron microscopic (TEM) images, high-resolution transmission electron microscopic (HRTEM) images, high angle annular dark field scanning TEM (HAADF STEM) images and energy dispersive spectrum (EDS) were taken using an ultra-high resolution field emission gun transmission electron microscope (JEM-ARM 200F, Jeol, Japan). X-Ray powder diffraction (XRD) was carried out on a Rigaku (Japan) D/max -γA X-ray diffractometer with Cu-Kα radiation (λ = 0.154178 nm). UV-vis diffuse-reflectance spectrum was recorded with a UV-2450 spectrophotometer in the wavelength range of 200-800 nm at room temperature. $BaSO_4$ was used as the reflectance standard material. The X-Ray photoelectron spectroscopy (XPS) was performed on a Perkin-Elmer RBD upgraded PHI-5000C ESCA system. Nitrogen adsorption/desorption measurements were performed at 77 K using a Micromeritics Tristar II 3020 M analyzer after the samples were degassed at 180 ºC for 6 h. The Brunauer-Emmett-Teller (BET) surface area was estimated by using adsorption data in a relative pressure range from 0.05 to 0.3. IR spectrum was recorded on a Niclolet AVATAR-360 IR spectrometer.

Test of photocatalytic activity

RhB (or MB) was chosen to measure photocatalytic performance of the obtained samples under solar light irradiation. 500 W Xe lamp (PLS-SXE500/500UV, Trusttech Co., Ltd. Beijing) was acted as light source. The reaction was maintained at room temperature by a cooling water circulation. 100 mg of the photocatalyst mixed with 20 mg/L of RhB (or MB) (100 mL) and formed a suspension for the following degradation reaction at room temperature. Prior to irradiation, stir the suspension in the dark for 30 min to reach an adsorption-desorption equilibrium. Then illuminate the suspension using the Xe lamp coupled with a 400 nm UV cut-off filter under magnetic stirring. At appropriate intervals, withdraw 4 mL suspension, centrifuge and remove the photocatalyst. Monitor the concentration of RhB (or MB) solution using UV-Vis spectrophotometer. The photocatalyst was centrifuged and used directly for the next experiment after each cycle in order to measure the stability of photocatalyst.

The experiments of trapping active species are similar to the photocatalytic tests. Scavengers t-butanol, p-benzoquinone (BQ) and ammonium oxalate (AO) were added into RhB solution to trap hydroxyl radicals (•OH), the superoxide radicals ($\cdot O_2^-$) and hole (h^+), respectively, followed by the photocatalytic tests.

All the photocatalytic experiments in this article were carried out at neutral pH.

Results and discussion

Characterization of photocatalysts

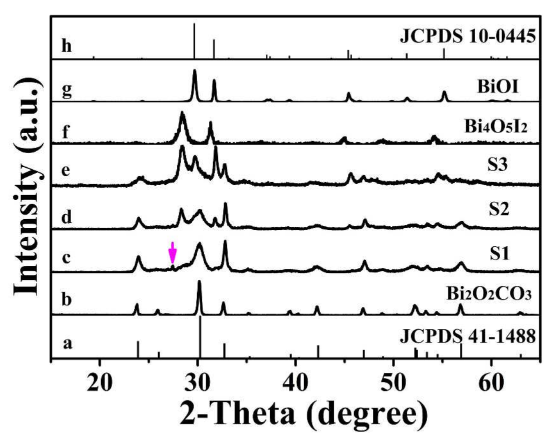

Fig. 1 XRD patterns of (a) standard card of $Bi_2O_2CO_3$; (b) pure $Bi_2O_2CO_3$ nanosheets; (c-e) S1, S2 and S3 heterostructures, respectively; (f) pure $Bi_4O_5I_2$ nanosheets; (g) pure BiOI nanosheets; (h) standard card of BiOI.

$BiOI/Bi_4O_5I_2/Bi_2O_2CO_3$ samples were synthesized by low-temperature solution method. Bi_2O_3 nanorods (0.1 g) and KI (0.0094 g) were dispersed into deionized water (40 mL) under magnetic stirring for 30 min, and then $Bi(NO_3)_3{\bullet}5H_2O$ (0.0276 g) was added. After further stirring for 30 min at room temperature, the mixture was transferred to the flask and heated at 80 ºC for 2 h. The obtained samples were labelled S1, S2 and S3 when the molar ratio of Bi_2O_3 : I^- : Bi^{3+} is 7.5 : 1 : 1, 7.5 : 2 : 2. and 7.5 : 3 : 3, respectively. Fig. 1 shows the X-ray powder diffraction (XRD) patterns of pure BiOI, $Bi_2O_2CO_3$, $Bi_4O_5I_2$ and the obtained heterostructures with different molar ration of $Bi_2O_3/I^-/Bi^{3+}$. All the diffraction peaks (Fig. 1b) can be indexed to the standard tetragonal $Bi_2O_2CO_3$ phase (JCPDS No. 41-1488) (Fig.1a). When the molar ratio of $Bi_2O_3/I^-/Bi^{3+}$ is 7.5 : 1 : 1 (S1 sample), the diffraction peaks of Bi_2O_3 nanorod precursor nearly disappear (see red arrow in Fig. 1c) and new peaks appear, which are ascribed to tetragonal $Bi_2O_2CO_3$ phase. Increase the molar ratio of $Bi_2O_3/I^-/Bi^{3+}$ to 7.5 : 2 : 2 (S2 sample), another two sets of diffraction peaks appear except $Bi_2O_2CO_3$ peaks (Fig. 1d), and the peaks of Bi_2O_3 disappears completely. The diffraction peak at 2θ = 28.34 can be recognized as $Bi_4O_5I_2$ [27,28], which can be proved by the XRD pattern of pure $Bi_4O_5I_2$ (Fig. 1f), and the peaks centred at 2θ = 29.64 and 31.65 are indexed to the tetragonal BiOI phase (JCPDS No. 10-0445). It also can be found from Fig. 1d that the intensity of $Bi_4O_5I_2$ peaks is obviously stronger than that of BiOI. Further increase the molar ratio of $Bi_2O_3/I^-/Bi^{3+}$ to 7.5 : 3 : 3 (S3 sample, Fig. 1e), the intensities of the diffraction peaks of BiOI become strong. However, the peaks of $Bi_2O_2CO_3$ and $Bi_4O_5I_2$ gradually decrease. According to above XRD analysis, we draw a conclusion that S2 and S3 samples are made of BiOI, $Bi_4O_5I_2$ and $Bi_2O_2CO_3$ three compositions. Though no obvious diffraction peaks of BiOI and $Bi_4O_5I_2$ appear, I element still exists in S1 sample, which can be proved by the following XPS analysis.

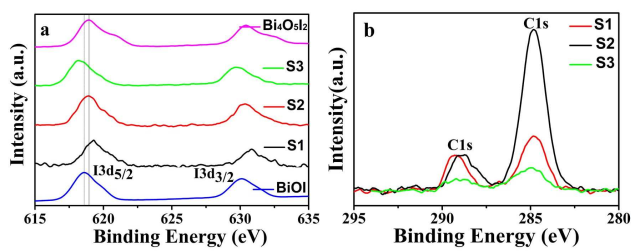

Fig. 2 XPS spectra for (a) I3d of the S1, S2, S3 and pure BiOI, $Bi_4O_5I_2$ samples, and (b) C1s of the S1, S2, S3 samples.

The X-ray photoelectron spectroscopy (XPS) was carried out to measure I and C elements in the obtained S1, S2 and S3 samples, as shown in Fig. 2. See carefully high-resolution XPS spectra of I3d in Fig. 2a, it can be found that I 3d5/2 and I 3d3/2 peaks obviously shift to the low binding energy from S1 to S3 samples. However, I 3d peaks in pure BiOI sample is located at low binding energy. So, it is proved that the content of BiOI is more and more, but $Bi_4O_5I_2$ is fewer and fewer from S1 to S3 sample. The C 1s peak (Fig. 2b) centred at 284.8 eV is ascribed to the signal from contaminant carbon[29], and the peak centred at 288.8 eV is assigned to the carbon of carbonate in $Bi_2O_2CO_3$. [30-32] The atom ratio of C (288.8 eV) : I in S1, S2 and S3 is 15 : 1, 5 : 1 and 2 : 1, respectively. This result shows $Bi_2O_2CO_3$ content obviously decreases from S1 to S3 sample. According to XPS results, combined with the result of XRD analysis, it can be drawn a conclusion that S1, S2 and S3 all consist of BiOI, $Bi_4O_5I_2$ and $Bi_2O_2CO_3$. The content of $Bi_2O_2CO_3$ obviously decreases, but oxyiodide BiOI and $Bi_4O_5I_2$ increase from S1 to S3 sample. The relative content of BiOI in oxyiodide gradually increases from S1 to S3.

pH value has more important effect on the formation of bismuth oxyiodides [33,34,15,16], the lower the pH value is, the lower O : I ratio is observed in the obtained bismuth oxyiodides (BiOI, $Bi_4O_5I_2$, $Bi_7O_9I_3$ and Bi_5O_7I).[15] BiOI and $Bi_4O_5I_2$ mixtures can be obtained when the pH value is varied from 5 to 10.[16] The initial pH values of the reaction system for S1, S2 and S3 samples before reaction are 5.75, 5.70 and 5.53, respectively. These pH values are beneficial for the formation of BiOI and $Bi_4O_5I_2$. Lower pH value (pH = 5.53) is favourable to the formation of BiOI, so that the contents of BiOI in S3 is obviously higher than in S1 and S2.

According to above analysis, it can be said that S1, S2 and S3 samples are all BiOI/ $Bi_4O_5I_2$/ $Bi_2O_2CO_3$ heterostructures.

SEM images of the Bi_2O_3 precursor and the obtained products S1, S2 and S3 are shown in Fig. S1. The Bi_2O_3 precursor is porous nanorod-like structure with diameter of 500 nm. The as-made S1 sample is one-dimensional flower-like structure with diameter of 500-1000 nm. The flower is made of many thin nanosheets. The shapes of S1, S2 and S3 have no obvious change.

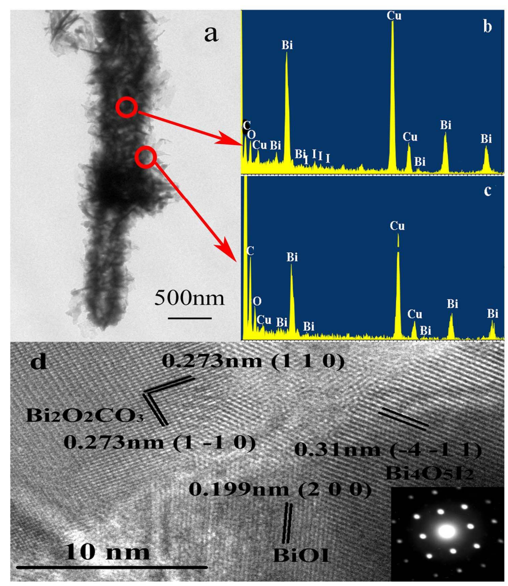

Fig. 3 TEM image (a), EDS spectra (b-c), HRTEM image (d) of the S2 heterojunction.

To further obtain the structural information of the obtained samples, S2 was characterized by the transmission electron microscopy (TEM). As shown in Fig. 3a, it can be clearly seen that many nanosheets consist of one-dimensional structure, which is consistent with the SEM result. It is also found that S2 sample is really a hollow structure, which is due to the Kirkendall effect.[35] The energy dispersive spectroscopy (EDS) analysis was carried out at different positions of S2 sample, as shown in Fig. 3b, c. It can be seen that Bi, O, I and C elements are co-presence if the electron beam irradiates on the middle region (see arrow inset Fig. 3c) of S2. However, there are only Bi, O, and C elements if the electron beam irradiates on the edge of S2 sample. Above results indicate that $Bi_2O_2CO_3$ nanosheets grow on the surface of S2 sample. Fig. 3d shows the high-resolution transmission electron microscopic (HRTEM) image taken from the S2. The interplanar spacing of lattice fringes is 0.273 nm, which can be indexed into the (110) lattice planes of tetragonal $Bi_2O_2CO_3$. And the spacing of the lattice fringes was about 0.199 and 0.31 nm, corresponding to the (200) planes of tetragonal BiOI and (-4-11) planes of monoclinic $Bi_4O_5I_2$.[16] The selected area electron diffraction (SAED) pattern (inset in Fig. 3d) taken from the $Bi_2O_2CO_3$ nanosheet is indexed as a $Bi_2O_2CO_3$ single crystal recorded along the [001] zone axis. Above results further prove that S2 is BiOI/ $Bi_4O_5I_2$/ $Bi_2O_2CO_3$heterostructures.

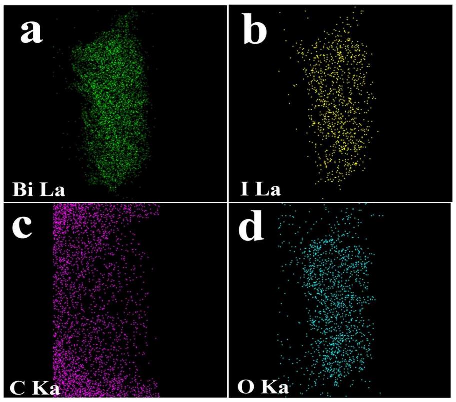

Fig. 4 The EDS element mapping of Bi, I, C and O, respectively.

Further analysis using dark-field scanning TEM (STEM) (Fig. 4) reveals contrast indicative of variations in the chemical composition as expected for the BiOI/$Bi_4O_5I_2$/$Bi_2O_2CO_3$ structure. STEM energy-dispersive X-ray spectroscopy (EDS) mapping of the same region (Fig. 4) defines clearly the spatial distributions of Bi, I, C and O in individual structure and illustrates that I elements mainly distributes into the centre of BiOI/$Bi_4O_5I_2$/$Bi_2O_2CO_3$ heterostructure (Fig. 4b). According to the distribution of C elements (Fig. 4c), it can be confirmed that $Bi_2O_2CO_3$ nanosheets grow on the surface of BiOI/$Bi_4O_5I_2$/$Bi_2O_2CO_3$ heterojunction, which is consistent with TEM result.

The formation mechanism of photocatalysts

In order to study the growth process of S2 sample, XRD patterns of samples obtained at different reactive time are shown in Fig. S2. When the reaction time is only 5 min, the strong diffraction peaks of BiOI appear except the peaks of Bi^{3+} hydrolysis product and Bi_2O_3 nanorods, no other peaks, such as $Bi_4O_5I_2$ or $Bi_2O_2CO_3$ can be found. The colour of the sample obtained at 5 min is orange red, which also proves the formation of many BiOI. Prolonging reaction time to 10 min, the new diffraction peaks indexed to $Bi_4O_5I_2$ appear except the peaks of Bi_2O_3 and BiOI. However, the peaks of Bi^{3+} hydrolysis product disappear completely. With the reaction time increase from 15 to 25 min, three sets of diffraction peaks of $Bi_4O_5I_2$, BiOI and Bi_2O_3 all can be found in the XRD patterns, but the intensity of the Bi_2O_3 peaks become weaker and weaker. When reaction time reaches 30 min, the peaks of Bi_2O_3 disappear completely, and new diffraction peaks appear, which is indexed to $Bi_2O_2CO_3$. Further prolong reaction time to 2 h, three sets of diffraction peaks of $Bi_4O_5I_2$, BiOI and $Bi_2O_2CO_3$ all can be observed in the XRD patterns, but the diffraction peaks of $Bi_2O_2CO_3$ obviously increase. Above results imply that $Bi_2O_2CO_3$ nanosheets grow on the surface of the $Bi_4O_5I_2$, BiOI. The color of obtained products changes gradually from orange red (5 min) to yellow (30 min), which indicates that the BiOI obtained at 5 min takes part in chemical reaction at the subsequent reaction time.

Fig. S3 is shown the SEM images of products obtained at different reaction time. It can be seen that the morphologies of the as-made products are all one-dimensional rod-like structure and no obvious difference.

According to above analysis, the possible formation mechanism of BiOI/ $Bi_4O_5I_2$/ $Bi_2O_2CO_3$ heterojunction is shown in Scheme 1. When the KI is added into the solution containing Bi_2O_3 nanorods, I^- ions first adsorb on the surface of Bi_2O_3 nanorods. When the $Bi(NO_3)_3$ is added into the reaction system, the acid condition is formed due to the Bi^{3+} hydrolysis. And then Bi^{3+} hydrolysis product also adsorb on the surface of Bi_2O_3. A part of Bi^{3+} hydrolysis products will react with I^- in solution to form BiOI on the surface of Bi_2O_3 nanorods within 5 min. Meanwhile, the preferred outward diffusion of Bi^{3+} ions from Bi_2O_3 nanorods in acid condition react with adsorbed I^- ions to form BiOI, which leads to a net material flux across the composite interface due to the Kirkendall effect. During the reaction process (5-25 min), the concentration of H^+ gradually decreases due to Bi_2O_3rods dissolve, more $Bi_4O_5I_2$ will be formed, compared with BiOI.[15] Moreover, the obtained BiOI also react with Bi_2O_3 nanorods to form $Bi_4O_5I_2$.[15] When reaction time reaches 30 min, CO_2 from air will react with bismuth oxyiodide (BiOI or/and $Bi_4O_5I_2$) to form $Bi_2O_2CO_3$ on the surface of sample due to the favorable reaction condition, such as appropriate pH value, and similar layer structure between $Bi_2O_2CO_3$ and bismuth oxyiodide (BiOI and $Bi_4O_5I_2$). Therefore, hollow BiOI/ $Bi_4O_5I_2$/ $Bi_2O_2CO_3$ heterojunction is formed finally.

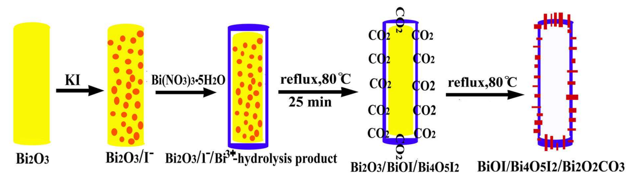

Scheme 1. Formation mechanism of one-dimensional hollow BiOI/$Bi_4O_5I_2$/$Bi_2O_2CO_3$ heterostructure.

The properties of the photocatlysts

The N_2 adsorption and desorption isotherm of BiOI/$Bi_4O_5I_2$/$Bi_2O_2CO_3$ heterojunction is measured, as shown in Fig. 5. The shape of the isotherm is a type IV with a type H3 hysteresis loop at high relative pressures according to the IUPAC classification, indicating the presence of mesoporous structure.[36,37] The pore size distribution of the samples are also estimated using the Barrett-Joyner-Halenda (BJH) method from the desorption branch of the isotherm, as shown in Fig. 5b. The size of mesopores is not uniform ranging from 2-20 nm. The smaller mesopores is ascribed to the pores within nanosheets, whereas larger ones can be correlated to the pores formed between stacked nanosheets. The BET surface areas of the samples were calculated and are summarized in Table 1. It can be found that BiOI and $Bi_4O_5I_2$ have the smallest and largest BET surface areas of 1.96 and 50.23 $m^2 \cdot g^{-1}$, respectively. BiOI/$Bi_4O_5I_2$/$Bi_2O_2CO_3$ heterostructures show large BET surface areas than pure BiOI and $Bi_2O_2CO_3$, and S2 sample own the largest BET surface area. The BET surface area has more effect on the photocatalytic performance of BiOI/$Bi_4O_5I_2$/$Bi_2O_2CO_3$ heterostructures, which can be found in the following photocatalytic experiments.

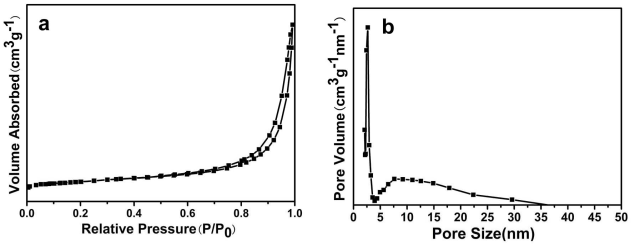

Fig. 5 (a) Nitrogen adsorption-desorption isotherm and (b) the corresponding pore size distribution of the S2 composite.

Table 1. Brunauer–Emmett–Teller (BET) surface area, band gap, valence band and conduction band and the pseudo-first-order rate constants for photodegradation of RhB and MB over photocatalysts.

Samples	A_{BET} ($m^2 \cdot g^{-1}$)	k (min^{-1}) (solar light) MB	(RhB)	k (h^{-1}) (visible light) RhB	Eg (eV)	VB (eV)	CB (eV)
S1	13.92	0.02866	0.03096	0.402			
S2	36.29	0.06866	0.08407	0.784			
S3	35.32	0.03575	0.03529	0.554			
$Bi_4O_5I_2$	50.23	0.01331	0.0086	0.308	2.33	1.01	-1.32
BiOI	1.96	0.00269	0.0020	0.043	1.78	1.42	-0.36
$Bi_2O_2CO_3$	8.90	0.00304	0.0034	0.065	3.33	2.02	-1.31

The optical property of pure BiOI, $Bi_4O_5I_2$, $Bi_2O_2CO_3$ and $BiOI/Bi_4O_5I_2/Bi_2O_2CO_3$ heterojunctions was examined using UV-vis diffuse-reflectance spectrum (DRS) (Fig. 6). The absorption edge of all $BiOI/Bi_4O_5I_2/Bi_2O_2CO_3$ heterojunctions appears in the range of 540~650 nm, and is red-shift gradually from S1 to S3, which is due to the content of the loaded-BiOI increase in the heterojunction. The color of the $BiOI/Bi_4O_5I_2/Bi_2O_2CO_3$ heterojunction also changes from light yellow (S1) to orange red (S3) with the loaded-BiOI content increase (inset in Fig. 6a).

The optical band gap of BiOI, $Bi_4O_5I_2$ and $Bi_2O_2CO_3$ can be calculated from the absorption spectra using the equation $\alpha h\nu = A\ (h\nu - Eg)^{2/n}$, in which α, hν, A, and Eg are the absorption coefficient, planck constant, light frequency, a constant and band gap, respectively.[38] In the equation, n decides the characteristics of the transition in a semiconductor, here n = 4 for these three samples. The energy of the band gap is calculated by extrapolating the straight line to the abscissa axis. The estimated band gap energies of the samples are 1.78 eV for BiOI, 2.33 eV for $Bi_4O_5I_2$ and 3.33 eV for $Bi_2O_2CO_3$ (Fig. 6b, Table 1).

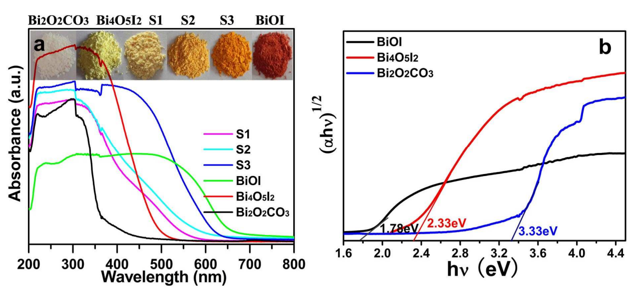

Fig. 6 (a) Diffuse reflectance spectra of different samples and (b) the plots of $(\alpha h\nu)^{1/2}$ vs. (hν) of BiOI, $Bi_4O_5I_2$ and $Bi_2O_2CO_3$ samples.

The photocatalytic performance of photocatalysts

The photocatalytic activity of the as-prepared $BiOI/Bi_4O_5I_2/Bi_2O_2CO_3$ heterojunctions, pure BiOI, $Bi_4O_5I_2$ and $Bi_2O_2CO_3$ was evaluated by degrading RhB dye in aqueous solution under solar light irradiation. Fig. 7a displays the correlation curves between the concentration of RhB dye and the irradiation durations in the presence of photocatalysts. It can be found that $BiOI/Bi_4O_5I_2/Bi_2O_2CO_3$ heterojunctions display much better photocatalytic activity than individual BiOI, $Bi_4O_5I_2$ and $Bi_2O_2CO_3$. And S2 samples exhibit the highest photocatalytic activities, which can degrade 100% RhB in 45 min under solar light irradiation. Fig. 7(b) displays the linear relationship between $\ln(C_0/C)$ and irradiation time, suggesting that the photocatalytic degradation reaction of RhB over the as-prepared catalysts should belong to the first-order kinetic relation. The calculated reaction rates have been shown in Table 1. The reaction rate constant of 0.084 min^{-1} for S2 sample is as 40, 25 and 10 times as ones for BiOI, $Bi_2O_2CO_3$ and $Bi_4O_5I_2$. The enhanced photocatalytic activity of BiOI/ $Bi_4O_5I_2$/ $Bi_2O_2CO_3$ heterostructure is ascribed to the formation of p-n-p junctions among BiOI, $Bi_2O_2CO_3$ and $Bi_4O_5I_2$ semiconductors, which could effectively reduce the recombination probability of photo-generated electrons and holes through internal electric field, improving the photocatalytic efficiency.

The photocatalytic activity of the samples was further evaluated by degradation of RhB dye under visible light irradiation (λ ≥ 400 nm). As shown in Fig. S4, S2 sample displays the highest photocatalytic activity among all the photocatlaysts for the degradation of RhB aqueous solution, and RhB can be completely decolored in 3 h under visible light irradiation. The reaction rate constant of 0.784 h^{-1} for S2 sample is as 20, 12 and 2.5 times as ones for BiOI, $Bi_2O_2CO_3$ and $Bi_4O_5I_2$ (see Table 1). Compared with BiOI heterostructures[39] and $Bi_7O_9I_3$/reduced graphene oxide[25], $BiOI/Bi_4O_5I_2/Bi_2O_2CO_3$ heterojunction exhibits high photocatalytic activities.

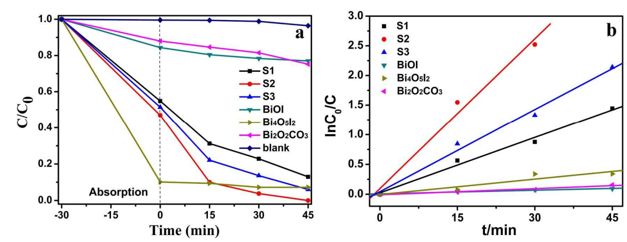

Fig. 7 (a) The degradation curves of RhB (20 mg/L), (b) Relevant degradation rates in the presence of as-prepared samples under solar light irradiation.

From Fig. 7a, we also find that $Bi_4O_5I_2$ exhibits stronger adsorptive ability for RhB molecules than S2 sample due to its largest BET surface (Table 1). We measure the IR spectra of the $Bi_4O_5I_2$ and S2 sample before and after photocatalysis. As shown in Fig. 8, some characteristic peaks of RhB,[40] such as 1590 cm^{-1}, 1467 cm^{-1},1414 cm^{-1}, 1341 cm^{-1} and 1132 cm^{-1}, are observed in the IR spectrum of $Bi_4O_5I_2$-RhB ($Bi_4O_5I_2$ after photocatalysis). However, the characteristic peaks of pure RhB are disappeared completely in the IR spectrum of S2-RhB (S2 after photocatalysis). These results show that S2 can completely degrade RhB under visible/solar light irradiation, but $Bi_4O_5I_2$ can't. Most of RhB molecules are only adsorbed on the surface of $Bi_4O_5I_2$ but not degraded after light irradiation, which can be proved by the photographs inset in Fig. 8. Compared with S2 sample, $Bi_4O_5I_2$ also displays strong adsorptive ability and weak photocatalytic activity for MB molecules, which can be seen from degradation curve of MB (Fig. S5) and relevant degradation rates (Table 1) in the presence of the obtained samples.

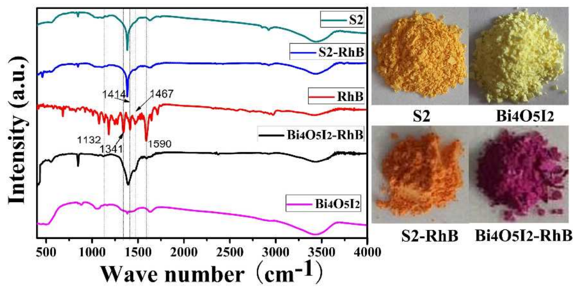

Fig. 8 IR spectra of the pure RhB dye, $Bi_4O_5I_2$ and S2 before and after photocatalysis.

To investigate the stability of photocatalytic performance in solar light region, the S2 sample was used to degrade RhB dye in 10 repeated cycles, and the results are shown in Fig. 9. It is noteworthy that S2 photocatalyst exhibits good photostability under solar light irradiation (Fig. 9a), and its photocatalytic efficiency has no decrease after 10 repeated cycles. From the XRD pattern (Fig. 9b), it can be found that the crystal phase of S2 sample is still $BiOI/Bi_4O_5I_2/Bi_2O_2CO_3$ heterojunction, demonstrating its high stability in the process of photocatalysis.

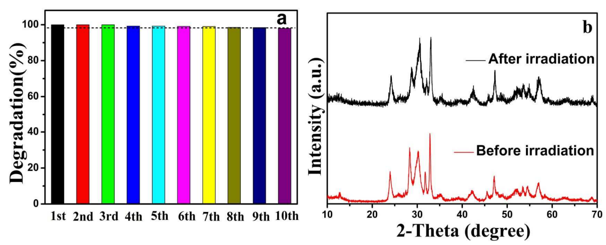

Fig. 9 Cycling runs in the photodegradation of RhB in the presence of S2 heterostructure under solar light irradiation.

The possible photocatalytic mechanism

The trapping experiments of active species during the photocatalytic process were carried out. Benzoquinone (BQ), tertbutyl alcohol (TBA), and ammonium oxalate (AO) were used as scavengers of superoxide radical (•O_2^-), hydroxyl radical (•OH) and h^+, respectively.[41–45] Fig. 10 shows the effect of different scavengers on the photodegradation rate over the S2 sample. It can be seen that the addition of TBA and BQ does not cause deactivation of S2 photocatalyst. However, the photocatalytic performance of S2 significantly decreases by the addition of AO (Fig. 10). These results suggest that h^+ is the main active species rather than •OH and •O_2^- radicals in the RhB photocatalytic process under solar light irradiation.

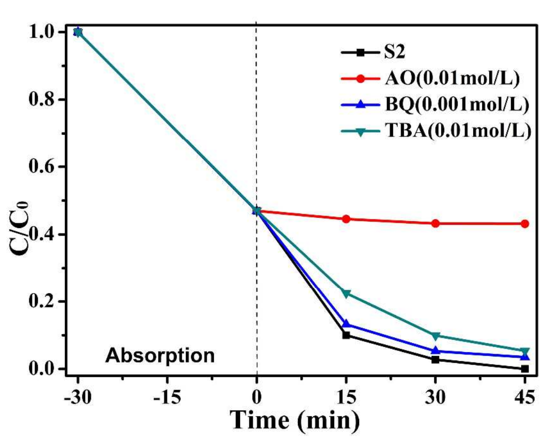

Fig. 10 Active species trapping experiments during the photocatalytic reaction for 45 min under solar light irradiation on S2 photocatalyst.

To determine the relative positions of conduction band (CB) and conduction band (VB) edges, the VB-XPS spectra of BiOI, $Bi_4O_5I_2$ and $Bi_2O_2CO_3$are measured and shown in Fig. 11. The VB edge of BiOI, $Bi_4O_5I_2$ and $Bi_2O_2CO_3$ is 1.42 eV, 1.01 and 2.02 eV, respectively. According to the VB edge of them, and combined with band gap derived from DRS, the CB edge potential of these three semiconductors can be obtained using the equation of $E_{CB} = E_{VB}$ - Eg. Relative data are listed in Table 1.

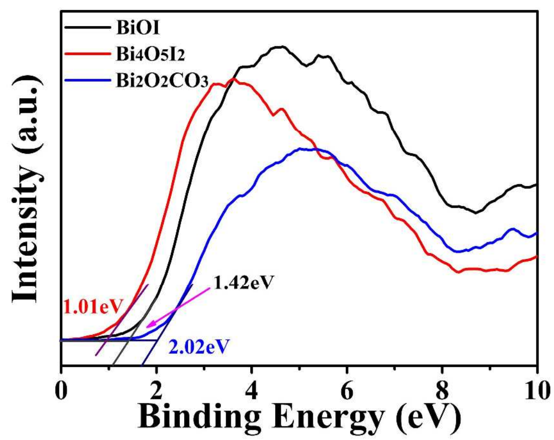

Fig. 11 VB-XPS spectra of BiOI, $Bi_4O_5I_2$ and $Bi_2O_2CO_3$.

Based on results of the trapping experiments and the VB-XPS data, we readily illustrate the band alignment of $BiOI/Bi_4O_5I_2/Bi_2O_2CO_3$ heterostructures and charge transfer (Fig. 12) under solar light irradiation. For p-type BiOI and $Bi_4O_5I_2$, their Fermi energy levels are close to the valence band, while for n-type $Bi_2O_2CO_3$, its Fermi energy level is close to the conduction band. When the three semiconductors are in contact to form p-n junction (Fig. 12b), there is diffusion of electrons from $Bi_2O_2CO_3$ to BiOI and $Bi_4O_5I_2$ due to their different Fermi energy level, resulting in accumulation of negative charges in BiOI and $Bi_4O_5I_2$ close to the junction. At the same time, the holes transfer from BiOI and $Bi_4O_5I_2$ to $Bi_2O_2CO_3$, leaving a positive section in $Bi_2O_2CO_3$ near the junction. Meanwhile, the energy bands of BiOI and $Bi_4O_5I_2$ shift upward along the Fermi level and those of the $Bi_2O_2CO_3$ shift downward along its Fermi level. With equilibration of BiOI, $Bi_4O_5I_2$ and $Bi_2O_2CO_3$ Fermi levels, the diffusion of electrons from $Bi_2O_2CO_3$ to BiOI and $Bi_4O_5I_2$ stops. Therefore, an equilibrium state is formed and two inner electric fields will also be generated at the interface. Under the solar/visible light irradiation, BiOI and $Bi_4O_5I_2$ with narrow band gap are excited and photoelectrons and holes are generated. The excited electrons on the conduction band of p-type BiOI and $Bi_4O_5I_2$ transfer to that of n-type $Bi_2O_2CO_3$, while the holes remain in the valence band of p-type BiOI and $Bi_4O_5I_2$. Furthermore, the migration rate of the photogenerated electrons and holes could be promoted by the internal electric field in the $BiOI/Bi_4O_5I_2/Bi_2O_2CO_3$ p-n-p heterojunctions and the photocatalytic activity is largely enhanced.

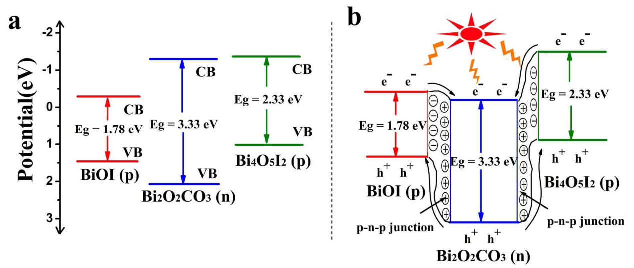

Fig. 12 Schematic diagram for (a) energy band of BiOI, $Bi_4O_5I_2$ and $Bi_2O_2CO_3$ and (b) the formation of p-n junction and the possible charge separation.

Conclusions

In summary, $BiOI/Bi_4O_5I_2/Bi_2O_2CO_3$ p-n-p junction photocatalysts have been prepared for the first time by low temperature solution method. The obtained $BiOI/Bi_4O_5I_2/Bi_2O_2CO_3$ p-n-p heterojunction exhibits higher photocatalytic activity than pure BiOI, $Bi_2O_2CO_3$ and $Bi_4O_5I_2$ for the degradation of RhB under solar/visible light irradiation. RhB (20 mg/L) can be completely degraded in 45 min/3 h under solar/visible light irradiation using S2 sample as photocatalyst. The reaction rate constant of 0.084 min^{-1} for S2 is as 40, 25 and 10 times as ones for BiOI, $Bi_2O_2CO_3$ and $Bi_4O_5I_2$ under solar light irradiation. This enhanced photocatalytic activity is due to the synergistic effects: (a) relatively large surface area improves the adsorption ability to RhB dye molecules; (b) the formation of p-n-p junction reduces the recombination of photo-generated electron-hole pairs by the internal electrostatic field in the junction region; (c) 1D ordered nanostructures is favourable for high efficient and directional transport and separation of electrons and holes. This work provides a facile and versatile strategy to fabricate $BiOI/Bi_4O_5I_2/Bi_2O_2CO_3$ p-n-p junction photocatalyst on a large scale.

Acknowledgements

This work is supported by the National Natural Science Foundation of China (21271165, 21101006).

Notes and references

1 Z. G. Zou, J. H. Ye, K. Sayama and H. Arakawa, *Nature,* 2001, **414**, 625–627.
2 M. G. Walter, E. L. Warren, J. R. McKone, S. W. Boettcher, Q. X. Mi, E. A. Santori and N. S. Lewis, *Chem. Rev*., 2010, **110**, 6446–6473.
3 S. N. Habisreutinger, L. Schmidt-Mende and J. K. Stolarczyk, *Angew. Chem. Int. Ed*., 2013, **52**, 7372–7408.
4 Q. Liu, Y. Zhou, J. H. Kou, X. Y. Chen, Z. P. Tian, J. Gao, S. C. Yan and Z. G. Zou, *J. Am. Chem. Soc*., 2010, **132**, 14385–14387.
5 W. G. Tu, Y. Zhou, Q. Liu, S. C. Yan, S. S. Bao, X. Y. Wang, M. Xiao and Z. G. Zou, *Adv. Funct. Mater.*, 2013, **23**, 1743–1749.
6 J. S. Lee, K. H. You and C. B. Park, *Adv. Mater.*, 2012, **24**, 1084–1088.
7 M. S. Zhu, P. L. Chen and M. H. Liu, *ACS Nano.,* 2011, **5**, 4529–4536.
8 W. Fan, Q. Zhang and Y. Wang, *Phys. Chem. Chem. Phys*, 2013, **15**, 2632–2649.
9 L. Li, P. A. Salvador and G. S. Rohrer, *Nanoscale Res. Lett*., 2014, **6**, 24–42.
10 H. Wang, L. Zhang, Z. Chen, J. Hu, S. Li, Z. Wang, J. Liu and X. Wang, *Chem. Soc. Rev*., 2014, **43**, 5234–5244.
11 Y. Peng, M. Yan, Q. G. Chen, C. M. Fan, H. Y. Zhou and A. W. Xu, *J. Mater. Chem. A*, 2014, **2**, 8517–8524.
12 J. Li, Y. Yu and L. Z. Zhang, *Nanoscale*, 2014, **6**, 8473–8488.
13 H. Cheng, B. Huang and Y. Dai, *Nanoscale*, 2014, **6**, 2009–2026.
14 L. Q. Ye, Y. R. Su, X. L. Jin, H. Q. Xie and C. Zhang, *Environ. Sci.: Nano*, 2014, **1**, 90–112.
15 X. Xiao, C. Liu, R. Hu, X. Zuo, J. Nan, L. Li and L. Wang, *J. Mater. Chem.*, 2012, **22**, 22840–22843.
16 X. Xiao, C. L. Xing, G. P. He, X. X. Zuo, J. M. Nan and L. S. Wang, *Appl. Catal. B: Environ.*, 2014, **148–149**, 154–163.
17 Q. C. Liu, D. K. Ma, Y. Y. Hu, Y. W. Zeng and S. M. Huang, *ACS Appl. Mater. Interfaces*, 2013, **5**, 11927–11934.
18 W. W. Lee, C. S. Lu, C. W. Chuang, Y. J. Chen, J. Y. Fu, C. W. Siao and C. C. Chen, *Rsc Adv.*, 2015, **5**, 23450–23463.
19 C. H. Liu and D. Zhang, *Appl Phys A-Mater*, 2015, **118**, 913–922.
20 J. Yang, L. J. Xu, C. L. Liu and T. P. Xie, *Appl Surf Sci.*, 2014, **319**, 265–271.
21 Y. R. Su, H. Wang, L. Q. Ye, X. L. Jin, H. Q. Xie, C. Z. He and K. Y. Bao, *Rsc Adv.*, 2014, **4**, 65056–65064.
22 J. Cao, X. Li, H. L. Lin, B. Y. Xu, B. D. Luo and S. F. Chen, *Mater Lett.*, 2012, **76**, 181–183.
23 X. Xiao, R. Hao, X. X. Zuo, J. M. Nan, L. S. Li and W. D. Zhang, *Chem. Eng. J.*, 2012, **209**, 293–300.
24 X. Xiao and W. D. Zhang, *Rsc Adv.*, 2011, **1**, 1099–1105.
25 H. Liu, Y. Su, Z. Chen, Z. T. Jin and Y. Wang, *J Mol Catal a-Chem*, 2014, **391**, 175–182.
26 S. J. Peng, L. L. Li, H. T. Tan, Y. Z. Wu, R. Cai, H. Yu, X. Huang, P. N. Zhu, S. Ramakrishna, M. Srinivasan and Q. Y. Yan, *J. Mater. Chem. A*, 2013, **1**, 7630–7638.
27 M. Schmidt, H. Oppermann, H. Bruckner and M. Binnewies, *Z. Anorg. Allg. Chem*., 1997, **623**, 1945–1953.
28 E. Keller, V. Krämer, M. Schmidt and H. Oppermann, *Z. Kristallogr.*, 2002, **217,** 256–264.
29 H. Q. Wang, Z. B. Wu and Y. Liu, *J. Phys. Chem. C*, 2009, **113**, 13317–13324.
30 A. Purkayastha, Q. Y. Yan, M. S. Raghuveer, D. D. Gandhi, H. F. Li, Z. W. Liu, R. V. Ramanujan, T. Borca-Tasciuc and G. Ramanath, *Adv. Mater.*, 2008, **20**, 2679–2683.
31 D. M. Chen, Z. Y. Jiang, J. Q. Geng, Q. Wang and D. Yang, *Ind. Eng. Chem. Res.*, 2007, **46**, 2741–2746.
32 H. Q. Sun, Y. Bai, Y. P. Cheng, W. Q. Jin and N. P. Xu, *Ind. Eng. Chem. Res.*, 2006, **45**, 4971–4976.
33 Y. Li, H. Yao, J. Wang, N. Wang and Z. Li, *Mater. Res. Bull.*, 2011, **46**, 292–296.
34 P. Rittner and H. Oppermann, *Z. Anorg. Allg. Chem.*, 1992, **617**, 131−135.
35 W. S. Wang, M. Dahl and Y. D. Yin, *Chem. Mater.*, 2013, **25**, 1179−1189.
36 H. G. Yu, R. Liu, X. F. Wang, P. Wang and J. G. Yu, *Appl. Catal. B*: *Environ.*, 2012, **111–112**, 326–333.
37 G. I. N. Waterhouse, G. A. Bowmaker and J. B. Metson, *Phys. Chem. Chem. Phys.*, 2001, **3**, 3838–3845.
38 M. A. Butler, *J. Appl. Phys.*, 1977, **48**, 1914−1920.
39 L. Q. Ye, X. D. Liu, Q. Zhao, H. Q. Xie and L. Zan, *J. Mater. Chem. A*, 2013, **1**, 8978–8983.
40 R. L. Liu, D. X. Xiao, Y. G. Guo, Z. H. Wang and J. S. Liu, *RSC Adv.*, 2014, **4**, 12958–12963.
41 G. V. Buxton, C. L. Greenstock, W. P. Helman and A. B. Ross, *J. Phys. Chem. Ref. Data.,* 1988, **17**, 513–886.
42 X. K. Li, N. Kikugawa and J. H. Ye, *Adv. Mater.,* 2008, **20**, 3816–3819.
43 L. Q. Ye, J. N. Chen, J. Y. Liu, T. Y. Peng, K. J. Deng and L. Zan, *Appl. Catal. B,* 2013,**130–131**, 1–7.
44 C. Wang, H. Zhang, F. Li and L. Zhu, *Environ. Sci. Technol.,* 2010, **44**, 6843−6848.
45 Y. Peng, Q. G. Chen, D. Wang, H. Y. Zhou and A. W. Xu, *CrystEngComm,* 2015, **17**, 569–576.

Synthesis of $BiOI/Bi_4O_5I_2/Bi_2O_2CO_3$ p-n-p heterojunctions with superior photocatalytic activities

Yin Peng*†, Pian-Pian Yu†, Hai-Yan Zhou† and An-Wu Xu*‡

One-dimensional $BiOI/Bi_4O_5I_2/Bi_2O_2CO_3$ p-n-p junction structure with superior photocatalytic activity was synthesized by simple low-temperature solution method.